PAPER

Check for updates

Understanding the effects of different loadings on properties of a silicon/carbon anode for lithium batteries

Yanyan Liu,[a] Zhongjun Shu,*[a] Qianqian Wang,[b] Jie Wu,*[ac] Wanzheng Lu, [ID] *[a] Qin Wang,[d] Aoqi Wang,[a] Yifan Ding[a] and Mingkun Ma[a]

Battery cells based on different silicon/carbon (Si/C) loadings were assembled in this work. Their battery performance, in particular their capacity and cycling stability, was evaluated. The battery was assembled in a way that a pure Li metal counter electrode, $LiPF_6$ liquid electrolyte and pole piece with Si/C coatings were employed. Standardized differential capacity curves (dQ_m/dV curves) revealed a redox reaction resulting from the intercalation/deintercalation process of lithium ions. The first coulombic efficiencies and capacity retention were greatly affected by Si/C loading. Moderate rather than minimum or maximum Si/C loading for lithium batteries showed the best electrochemical performance. In addition, electrochemical impedance spectroscopy (EIS) quantified the resistances of organic electrolytes and the solid electrolyte interface (SEI). Mechanism analysis was conducted by drawing support from battery disassembly technology and material analysis methods. Notably, the phase and structure of Si/C anode materials undergoing charging and discharging were characterized. Raman spectra demonstrated that the charging and discharging processes significantly weaken the characteristics of Si owing to the formation of an Li_xSi alloy compound. The morphology and difference in electrode expansion of the anode with different Si/C loadings caused by long charge–discharge cycles were analyzed using scanning electron microscopy (SEM). Besides, elemental analysis results indicated that silicon lithium alloying is more prone to oxidation. It is proposed that this work could help provide a basis for the rational design of Si/C pole pieces for lithium batteries.

1. Introduction

Lithium batteries are widely used in electronic equipment, electrochemical energy storage power stations, and electric vehicles because of their high energy density and long cycle life.[1] The energy density of lithium-ion batteries depends on cathode and anode active materials. Despite the continuous optimization of active materials, the actual energy density of the battery pack is still not enough to meet the needs of products powered by lithium batteries in terms of weight and volume.[2,3] In recent years, new high-capacity anode electrode materials have emerged successively, although research on anode electrodes has been relatively overlooked. However, numerous scholars are increasingly realizing that improving the capacity of anode materials or designing new high-capacity anode materials is crucial for the development of high-performance lithium batteries, which has become one of the major issues in the field of lithium batteries.[4,5]

Currently, graphite is the most widely used anode material for lithium batteries. Nevertheless, graphite suffers from the disadvantage of low capacity (372 mA h g^{-1}). Silicon has the advantages of high specific capacity (4200 mA h g^{-1}), medium potential, environmental friendliness, and low cost and is a very promising anode material for improving the energy density of lithium-ion batteries.[6] However, poor conductivity and significant expansion/contraction changes are undeniable drawbacks that severely hinder its development.[7] Compared with traditional graphite materials and pure silicon, silicon/carbon (Si/C) composites have a relatively high specific capacity (much higher than graphite), which can significantly improve the energy capacity of lithium batteries and extend the overall service life of lithium batteries.[8] Additionally, Si/C composite anode materials have a faster ion transmission speed (than pure silicon), which can improve the charge–discharge rates of lithium batteries, making it suitable for scenarios with high demand for fast charging.[9] In this scenario, Si/C materials are widely regarded as the most promising new anode electrode material.

[a]School of Safety Science and Engineering, Changzhou University, Changzhou 213164, Jiangsu, China. E-mail: shuzhongjun119@126.com; wujie@cczu.edu.cn; luwanzheng@cczu.edu.cn

[b]School of Energy and Power Engineering, University of Shanghai for Science and Technology, Shanghai 200093, China

[c]College of Safety Science and Engineering, Nanjing Tech University, Nanjing 211816, Jiangsu, China

[d]Hubei Wanrun New Energy Technology Co., Ltd, Shiyan 442500, Hubei, China

Nowadays, the Si/C loading (*i.e.*, active substance loading) per unit area or the thickness of the pole piece is generally neglected, the increase in Si/C loadings has a positive correlation effect on the performance of lithium batteries,[10] but it can always be accompanied by the serious deterioration of electrochemical properties due to thickness.[11] A study proposes a high-loading silicon anode electrode without carbon additives, which significantly improves the cycling and service life of the battery by solving the interface problem between the silicon anode electrode and the electrolyte.[12,13] This high-loading silicon anode electrode design achieves high energy density by minimizing the ratio of binder and conductive additives, while introducing sulfur compound electrolytes.[14,15] The latest structural design, synthesis routes, and electrochemical properties of silicon/carbon composite anode electrode materials were studied, such as core–shell structure, eggshell structure, porous structure, and embedded structure. Silicon/carbon matrix composites are used as an important method to improve the electrochemical performance.[16] These structural designs not only improve the conductivity of silicon, but also alleviate the volume expansion problem of silicon during charging and discharging processes, but require material modification.[17,18] A high-tap-density carbon-coated sub-nano-Si-embedded activated carbon (ACSC) was developed with the aim of achieving high volume capacity and long cycling performance.[19] Atomic level mixed silicon/carbon was used to ensure isotropic expansion and structural stability, while the formation of crystalline $Li_{15}Si_4$ is reduced by the stress voltage coupling effect,[20] thereby improving the cycling stability of the battery.[21] The difficulty of operation and high requirements for material modification are the shortcomings of such methods.[22–24] Adjusting the silicon carbon density and optimizing the material structure are used to enhance the silicon carbon loading capacity, which can significantly improve the performance of silicon carbon lithium batteries. Material modification and coating structures were taken as the starting point of research,[25] providing the possibility for developing lithium batteries with higher energy density and better cycling stability. Moreover, opening up new perspectives to enhance silicon carbon loadings not only has novelty in theory, but also has important significance in practical applications.[26] The most suitable matching relationship between Si/C loading and pole piece thickness has been sought by scholars to improve the specific capacity,[27,28] initial coulombic efficiency, and cycling stability of silicon-based anode electrodes for lithium batteries.[29] Once the technological bottleneck is overcome, the overall energy density of lithium batteries is improved and high-capacity silicon/carbon composite anode electrodes are valued, which have important research significance.[30]

Therefore, finding the optimal Si/C loading plays an important role in the preparation of Si/C anode layers.[31] In order to solve the above-mentioned problems, this work provides five types of battery cells with different Si/C loadings and comparatively studies their electrochemical performance. It is found that the 2.1 mg cm^{-2} loading battery cells can achieve a first coulombic efficiency of 88% and deliver a specific capacity of 550 mA h g^{-1} after 100 cycles. The two oxidation peaks located

at 0.37 V and 0.52 V can be observed on differential capacity curves, which is attributed to the formation of dealloying Li_xSi in an amorphous state. EIS reveals the effects of Si/C loading on electrolyte resistance, solid electrolyte interface (SEI) resistance, and charge transfer resistance. Besides, the intrinsic properties of Si/C pole pieces are discussed in detail. This study can contribute to the application of Si/C materials as anodes for lithium batteries.

2. Experimental

2.1 Materials and preparation

Carboxymethyl cellulose (CMC, transparent viscous adhesive solution) and polyacrylic acid (PAA, transparent plasticizer) were mixed in a mass ratio of 1/3 to obtain mixed liquid A. Si/C, conductive agent (Super P), and the mixed liquid A in a mass ratio of 7/2/1 were mixed in an appropriate amount of deionized water using a mixer (THINKT Corporation, ARM-310) to obtain an anode slurry. The slurry was evenly coated on a clean copper foil using a knife coater (Hefei Kejing Material Technology Co., Ltd), and the coating thickness was controlled by rotating the graduation knob to change the distance between the scraper and the copper foil. In this work, the graduation knob reading to increase every 5 μm to obtain a set of pole pieces was set, with an initial graduation of 10 μm, thus obtaining 5 sets of pole pieces and then transferred to a vacuum box at 80 °C for 12 hours. The dried anode electrodes were cut into circular sheets and kept in a high-purity Ar glove box. To precisely characterize this series of pole pieces, a refined definition method is used, which is based on the Si/C loading per unit area, and the gradient relationship of coating thickness is transformed. The Si/C loading was installed at 1.0 mg cm^{-2}, 1.2 mg cm^{-2}, 2.1 mg cm^{-2}, 2.8 mg cm^{-2}, and 3.2 mg cm^{-2} (± error ≤ 0.1 mg cm^{-2}) labeled as samples 1, 2, 3, 4, and 5, respectively, and the pole pieces with five coating thicknesses were formed. A polyethylene (PE) separator was made into 19 mm circular pieces as a battery separator. A lithium metal sheet (size is 16 mm) was used as the counter electrode, and the formula for the electrolyte is 1 M $LiPF_6$ in DMC : EC : EMC = 1 : 1 : 1 vol% with 5% FEC and 1% VC. The battery specifications are CR-2032 coin battery cells. The assembly of all battery cells was fabricated in a high-purity Ar glove box.

2.2 Tests and characterization

The charge–discharge cycle test was carried out at a current density of 300 mA g^{-1} and a voltage of 0.02–2.0 V at 25 °C using a NEWARE battery test system. Electrochemical impedance spectra (EIS) were recorded using CHI760E (CH Instruments) in the range of 1 MHz–0.1 Hz at an amplitude of 5 mV, and an open circuit voltage was set to initial potential. The anode electrode samples were disassembled in a high-purity Ar glove box and cleaned with dimethyl carbonate (DMC). Transmission electron microscopy (TEM, FEI Tecnai F20) and X-ray diffraction spectroscopy (XRD, Rigaku Corporation) were performed to characterize the phase and structure of the electrode samples. Raman spectroscopy (LabRAM HR Evolution) was performed to

characterize functional groups. Scanning electron microscopy (SEM, ZEISS GeminiSEM 300) with electron dispersive spectroscopy (EDS) was performed to analyze the morphology, thickness, and elemental composition of the samples.

3. Results and discussion

The galvanostatic charge–discharge curves of the battery cells based on 1.0 mg cm^{-2} (Sample 1), 1.2 mg cm^{-2} (Sample 2), 2.1 mg cm^{-2} (Sample 3), 2.8 mg cm^{-2} (Sample 4), and 3.2 mg cm^{-2} (Sample 5) tested at 300 mA g^{-1} (around 0.462C, 1C = 650 mA g^{-1}) and 25 °C are shown in Fig. 1a. Samples 1 and 2 confirm that a slight increase in Si/C loading has little effects on the initial charge–discharge performance. The authors think that during the initial charge–discharge process of the battery cells, the electrolyte may be irreversibly decomposed, forming a solid electrolyte interface (SEI).[32] This process not only consumes Li$^+$ but also the SEI film formed may continue to consume lithium-ions in the subsequent charge–discharge process. Besides, the poor reversibility of lithium-ion deintercalation during charge–discharge processes can lead to an increase in the number of lithium-ion deactivations.[33] When the Si/C loading corresponding to Samples 2, 3, 4, and 5 increases significantly, two interesting findings are concluded. First, the initial coulombic efficiencies of these four groups of battery cells gradually declined in the order of Sample 2 > Sample 3 > Sample 4 > Sample 5. The thicker the electrode layer (with higher Si/C loading), the more lithium-ions enter the interior of the electrode layer, making it difficult to return and resulting in irreversible capacity and lower initial coulombic efficiency. However, the smallest Si/C loading pole piece (Sample 1) has the lowest initial coulombic efficiency of 67% since lithium-ions shuttle to the Si/C surface and form an extremely stable SEI film on the surface in a too thin electrode, making it difficult for lithium ions to return. Second, the capacity retention of all Si/C loading pole piece samples after 100 cycles continues to

improve (Sample 1 > Sample 2 > Sample 3 > Sample 4 > Sample 5), which may be because as the electrode thickness increases, the initial bonding process between lithium-ions and Si/C composite particles becomes more difficult. In addition, as the number of cycles increases, the activation of the battery material becomes increasingly sufficient. Nevertheless, it is worth mentioning that the high current of about 0.462C causes difficulties in the opening of the shuttle channel. Therefore, it is supposed that the capacity retention will continue to increase, and improving the conductivity is one way to solve this phenomenon.

The long-term cycling stability of these battery cells with different Si/C loadings at a current density of 300 mA g^{-1} is presented in Fig. 1b. It is worth noting that a phenomenon with a coulombic efficiency greater than 100% has been observed on the curve, and the design of battery assembly and testing steps has been explained by other scholars as the reason for this phenomenon. Usually, button batteries with lithium sheets as the counter electrode are used, and the lithium insertion reaction first occurs (reflected in the testing steps as discharge first and then charge, and an excess of lithium will migrate from the anode back to the lithium sheet after discharge), which is explained as the reason for this phenomenon. The above content provides a detailed explanation of how this phenomenon occurs from the experimental design, and potential factors such as measurement errors and side effects are also discussed. The size of the Si/C pole pieces in this work is 12 mm, while the size of the lithium electrode used as the counter electrode is 16 mm, and the electrolyte used also contains Li salts, which are the reasons for this phenomenon. In addition, authors considered whether the Si/C powder used in this study had undergone lithium powder pretreatment. The battery cells with low Si/C loadings, *i.e.*, Sample 1 and 2 deliver high specific discharge capacity over 100 charge–discharge cycles, which can achieve more than 600 mA h g^{-1}. The two sets of battery cells with moderate Si/C loading pole pieces (Samples 3 and 4) have
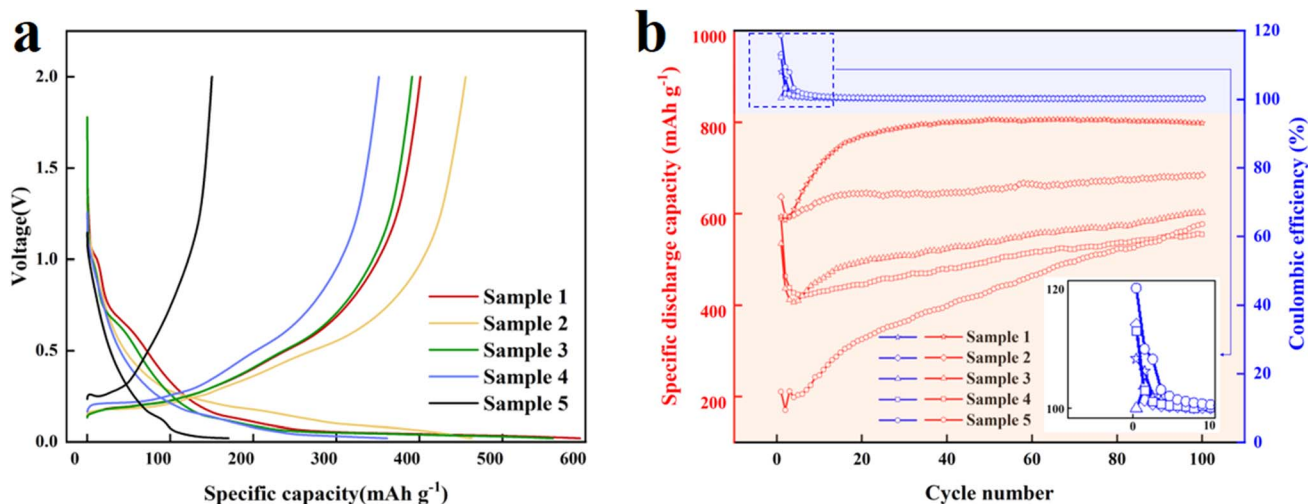

Fig. 1 Electrochemical performance of battery cells with different Si/C loadings at 300 mA g^{-1}: (a) initial charge–discharge curves and (b) cycling stability.

a relatively low specific discharge capacity of 550–600 mA h g^{-1}. However, Sample 5 with the largest Si/C loading pole piece can only provide the minimum specific discharge capacity. Apart from Sample 5, other samples demonstrate excellent cycling stability over 100 charge–discharge cycles. For all samples, the coulombic efficiencies reach around 100% after the 4th charge–discharge cycle.

The redox reaction caused by the intercalation/deintercalation process of lithium-ions is figured out by differential capacity curves. The standardized differential capacity curves (dQ_m/dV curves) are described in Fig. 2.

The Si/C powder used in this work is an unmodified conventional material on the market, which weakens the possibility of generating new compounds. By analyzing the previous research conclusions of scholars that Li$_x$Si alloys are compounds formed by the reaction of silicon and lithium,[34] where "x" represents the molar ratio of lithium to silicon.[16,35] The experiment was conducted at 25 °C, according to the referent[36–39] that complex alloys composed of Li$_x$Si alloys, Li$_x$SiO$_y$ (lithium–silicon oxide), SiO$_x$ (silicon oxide) was formed in our work. The reason for the appearance is explained in detail by the peaks in the dQ_m/dV curves. The initial dQ_m/dV curves related to the initial intercalation/deintercalation process of Li$^+$ demonstrate that the reduction peak near the 0.2 V position is due to the diffusion of Li$^+$ into silicon particles, forming an amorphous state of Li$_x$Si alloys via alloying reactions (Fig. 2a). This will cause significant volume expansion (up to 400%), which not only leads to electrode pulverization and poor cycling stability, but also causes failure contact between the active substance and the electrolyte. Correspondingly, after 100 charge–discharge cycles, it was found that the oxidation peak at 0.37 V can be explained as the formation of silicon dioxide (SiO$_x$) during the initial lithium insertion process (Fig. 2b). The problem of the initial coulombic efficiency and cycle life can be explained by the generation of silicon oxide (SiO$_x$). During the first lithium insertion, irreversible reactions occur with lithium in the electrolyte, producing inert phase silicon oxides (such as

Li$_2$O and Li$_4$SiO$_4$), resulting in low initial coulombic efficiency of the battery. However, its appearance can buffer the volume changes during the cycling process, which is beneficial for obtaining better performance and higher cycle life, and it is also well correlated with the experimental phenomena of this work. During the cycle, a new peak appeared on the oxidation peak located at 0.52 V, which is believed to be due to the decomposition of the electrolyte during the activation reaction and the formation of a stable SEI film, and this is also considered the fundamental reason for irreversible capacity loss and a low initial coulombic efficiency.[40]

For the battery cells with low Si/C loadings and excellent electrochemical performance, this work analyzes the transport behavior of lithium-ions through the EIS test. The Nyquist plots and equivalent circuit of the battery after 100 charge–discharge cycles are shown respectively in Fig. 3a and b. The Nyquist plots for Samples 1, 2, and 3 all consist of two compressed semicircles and an oblique straight line. The starting point of the Nyquist plots represents the resistance of the electrolyte (R_s). The former semicircle exists in high frequency and is represented by the resistance related to the SEI film (R_{SEI}). The second semicircle appears in the range from high frequency to mid-frequency and is used to study the relationship between electrode materials and electrolytes, commonly represented by charge transfer resistance (R_{ct}).[41] The latter oblique straight line can be used to evaluate and analyze the transfer process of lithium-ions in active materials, as represented by W_o.[42] Table 1 lists the resistances of R_s, R_{SEI}, and R_{ct}. All the samples show low resistance of the electrolyte, less than 4 Ω. The high Si/C loading thickens the electrode, resulting in greater SEI resistance (R_{SEI}) and charge transfer resistance (R_{ct}). The reason for this phenomenon can also be explained by the low thickness of the electrode plate, which facilitates particle shuttles. The impedance change of charge transfer between the anode and cathode electrodes exhibits a certain lag. The studies show that significant changes in charge–discharge states can easily affect the low-frequency
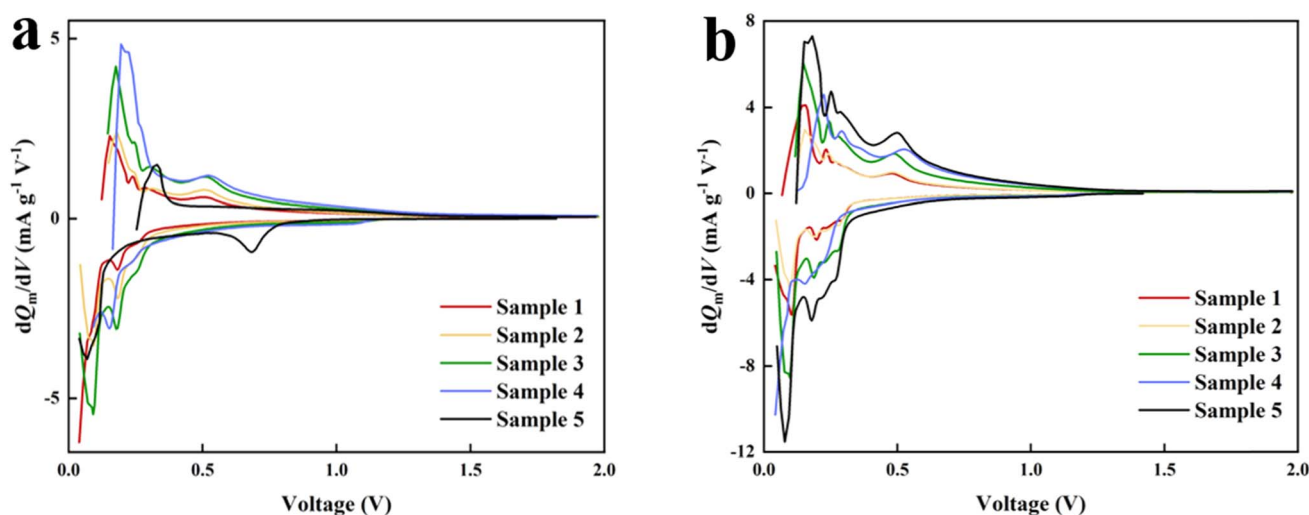

Fig. 2 Standardized differential capacity curves (dQ_m/dV curves): (a) initial and (b) for the 100th charge–discharge cycle.
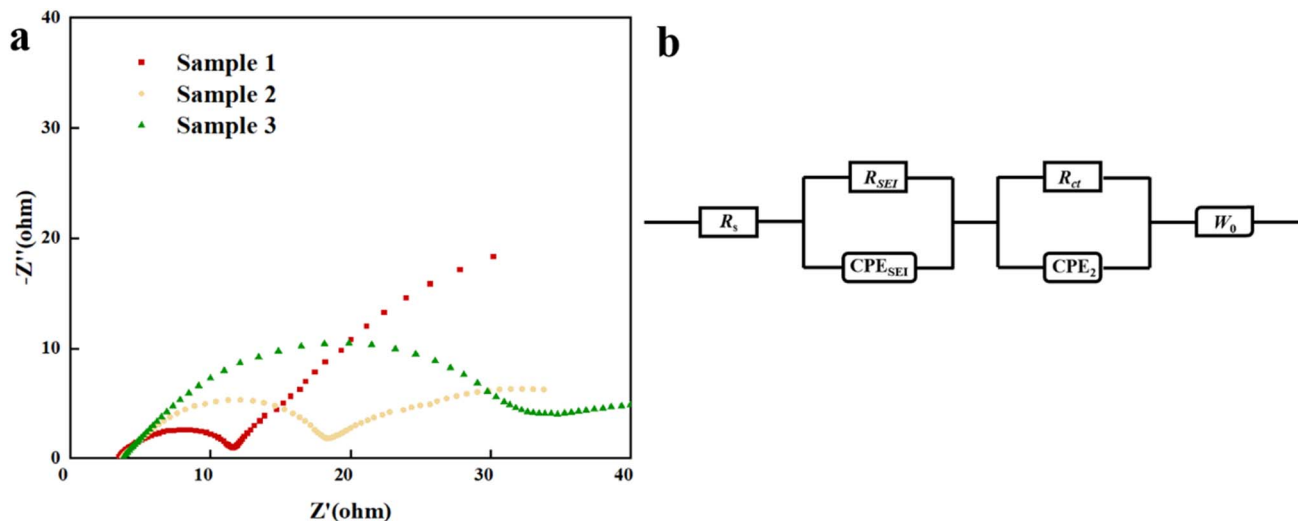
Fig. 3 (a) Nyquist plots and (b) equivalent circuit of the battery after 100 cycles at 300 mA g^{-1}.

Table 1 Summary of resistances: R_s, R_{SEI}, and R_{ct}

Sample	Si/C loading	R_s	R_{SEI}	R_{ct}
Sample 1	1.0 mg cm^{-2}	3.520	0.666	7.514
Sample 2	1.2 mg cm^{-2}	3.728	0.939	13.863
Sample 3	2.1 mg cm^{-2}	3.836	1.408	27.786

part, increasing the diffusion impedance of lithium ions in electrode materials and leading to battery capacity loss.[43]

In Fig. 4a–c, the internal structure of the pole piece is demonstrated by TEM images, and the phenomenon is obvious that silicon particles are uniformly dispersed in the carbon matrix of the pole piece, as observed from the images with clear and evenly distributed edges. The microstructure of the pole piece is also tested by HRTEM images shown in Fig. 4d. The lamellar distribution of Si/C is exhibited by their distinct lattice fringe, where cubic-Si belongs to the (2 2 0) plane with an interplanar spacing of 0.190 nm. C of the pole piece showed a close-packed hexagonal structure which is the (0 0 2) plane with 0.352 nm spacing. Hence, obvious boundaries could be seen at the interface between Si/C. Through HRTEM analysis, the lattice arrangement and crystal integrity of particles in the pole piece are revealed. At the same time, the distribution of silicon and carbon, as well as their relative content in particles, is mapped and shown in Fig. 4e. The relative contents of silicon (Si), carbon (C), and oxygen (O) are 39.48%, 10.26%, and 50.26%, respectively, as analyzed by EDS mapping of electrode materials. The distribution of silicon and carbon in the pole piece is revealed at this ratio, indicating that the carbon element dominates in the sample.

The phase evolution, chemical characteristics, and morphology are revealed by disassembling the battery and using material analysis methods. Fig. 5a and b respectively show the XRD patterns of the fresh Si/C pole pieces and Si/C pole pieces after 100 charge–discharge cycles. The Si/C sample

is uniformly coated on the copper foil, so the diffraction peaks at 43.4°, 50.5°, and 74.2° correspond to the (111), (200), and (220) crystal planes, respectively, with a high degree of coincidence with the standard card of Cu (PDF #85-1326).[44] The Si/C material exhibits strong diffraction peaks (002) and (004) at 26.4° and 54.6°, which partially overlap with the standard card of C (PDF #41-1487). A weak (452) splitting peak appears at 74.1°, which partially overlaps with the standard card of C (PDF #50-0927). It can be inferred that the content of C material in the Si/C material is relatively high.[45,46] According to the work, graphite has two relatively stable phases, namely hexagonal graphite (HG) and rhombohedral graphite (RG), and RG has poor stability, which is why weak peaks appear.[47] The weak (111) splitting peak appears at 28.276°, a coincidence with the standard card of Si (PDF #27-1402), indicating that the Si material content in the sample material is relatively low.

The Raman spectra of the fresh Si/C pole pieces and Si/C pole pieces after 100 charge–discharge cycles are displayed in Fig. 6a and b. All samples show a strong peak at 512 cm^{-1}, which is a typical Si element characteristic peak,[48] indicating the presence of Si in the composite material.[49] The spectral peaks at 1331 cm^{-1} and 1595 cm^{-1} belong to the D and G peaks of the carbon element, respectively. The higher the intensity of the D peak, the higher the degree of carbon disorder in the material. The stronger the G peak, the higher the degree of graphitization of carbon in the material. As the Si/C loading increases, the intensity of each peak decreases, which may be the reason for the decreasing degree of material disorder. In addition, it can be seen that the characteristic peaks of D, G, and Si elements in the samples significantly decrease after charge–discharge cycles, indicating the lithiation phenomenon of Si/C pole pieces after charge–discharge cycles (Fig. 6b). There are no characteristic peaks in the Raman shift spectra of the samples, indicating that the loading per unit area affects the degree of lithiation. Using the commonly used I_D/I_G values to determine the degree of graphitization of carbon materials, the average I_D/I_G of the
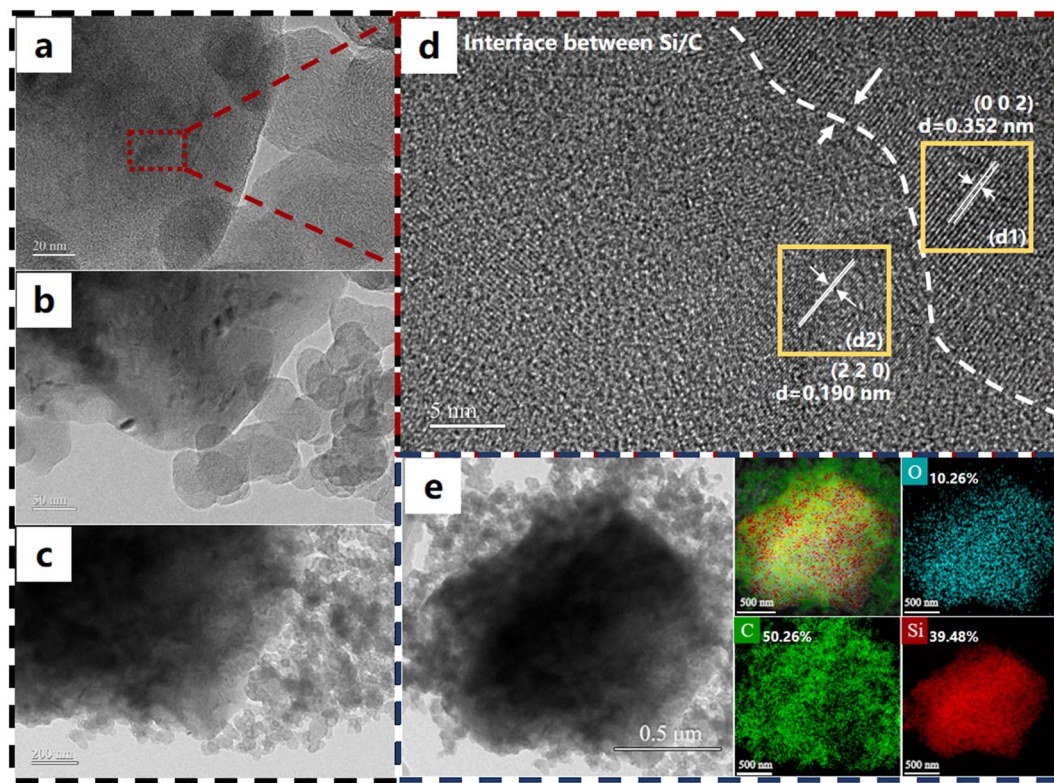
Fig. 4 Morphology diagram of the Si/C pole piece: (a) on a 20 nm scale; (b) on a 50 nm scale; (c) on a 200 nm scale; (d) HRTEM image. (e) Mapping results for the surface.
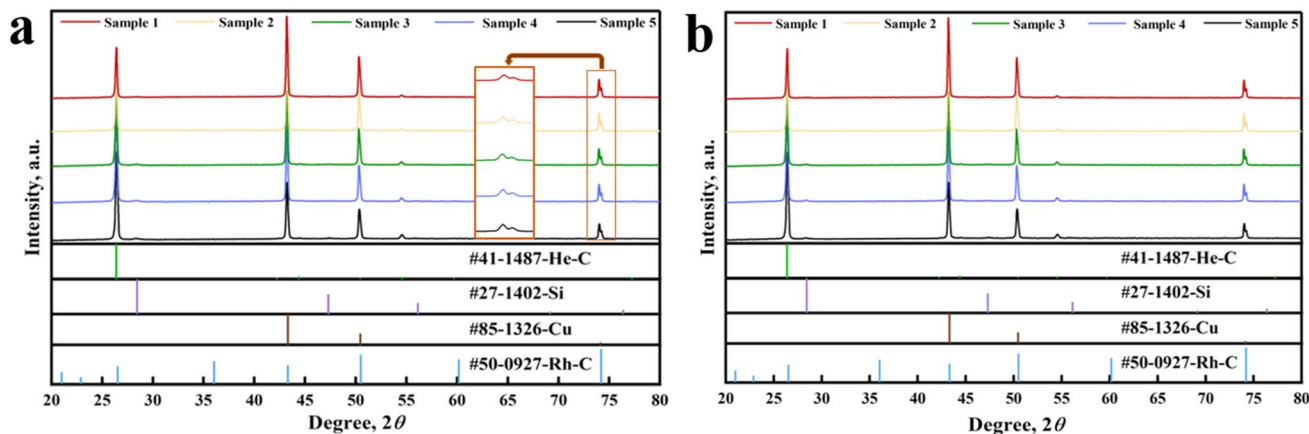

Fig. 5 XRD patterns of Si/C pole pieces with different Si/C loadings: (a) fresh and (b) after 100 cycles.

original electrode layers was calculated to be 1.08, while the I_D/I_G value of the electrode layers after charge–discharge cycles was 1.12. This indicates that the degree of graphitization of carbon materials has been improved to a certain extent, and it can be concluded that the degree of graphitization of the original Si/C material is relatively low, which may lead to defects in the structure.[50] The existence of defects can effectively shorten the transmission path of Li+ and improve the ion conductivity of materials to a certain extent. Compared with the original electrode, the peak intensity of the characteristic peak of Si after

cycling has weakened. The authors speculate that complex Li_xSi compounds are generated after discharge, and due to the extremely unstable behavior of lithium,[51] lithium is easily oxidized during battery disassembly, which may take away some Si and account for the decrease in Si content.

Fig. 7 displays the SEM images and mapping results of Si/C pole pieces after 100 charge–discharge cycles and the fresh Si/C pole pieces with different Si/C loadings for Samples 5, 4, 3, 2, and 1. Correspondingly, Si and O element contents before and after charging–discharging are presented in Table 2.
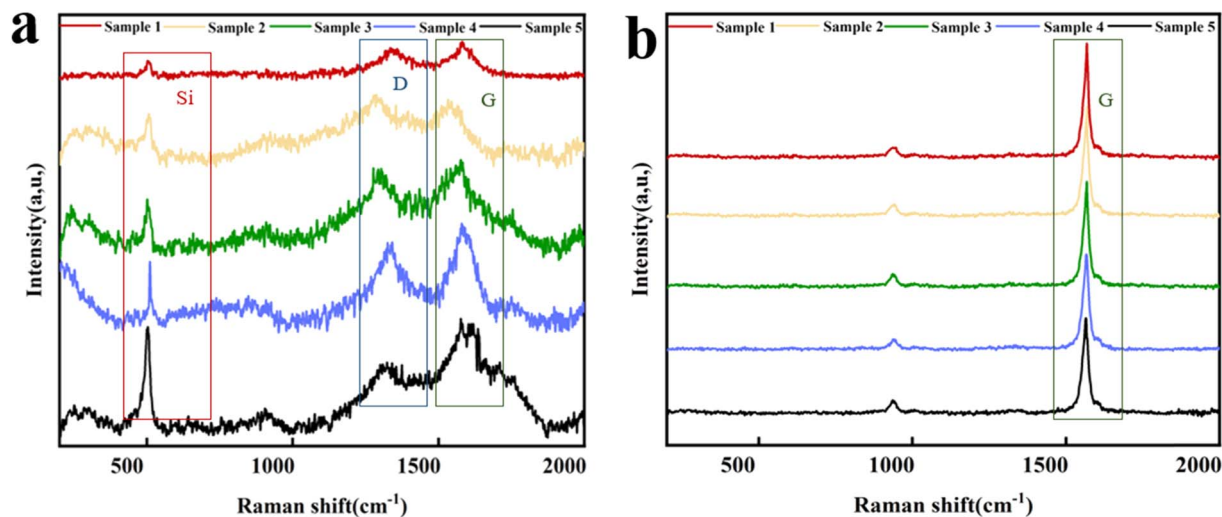
Fig. 6 Raman patterns of Si/C pole pieces with different Si/C loadings: (a) fresh and (b) after 100 cycles.
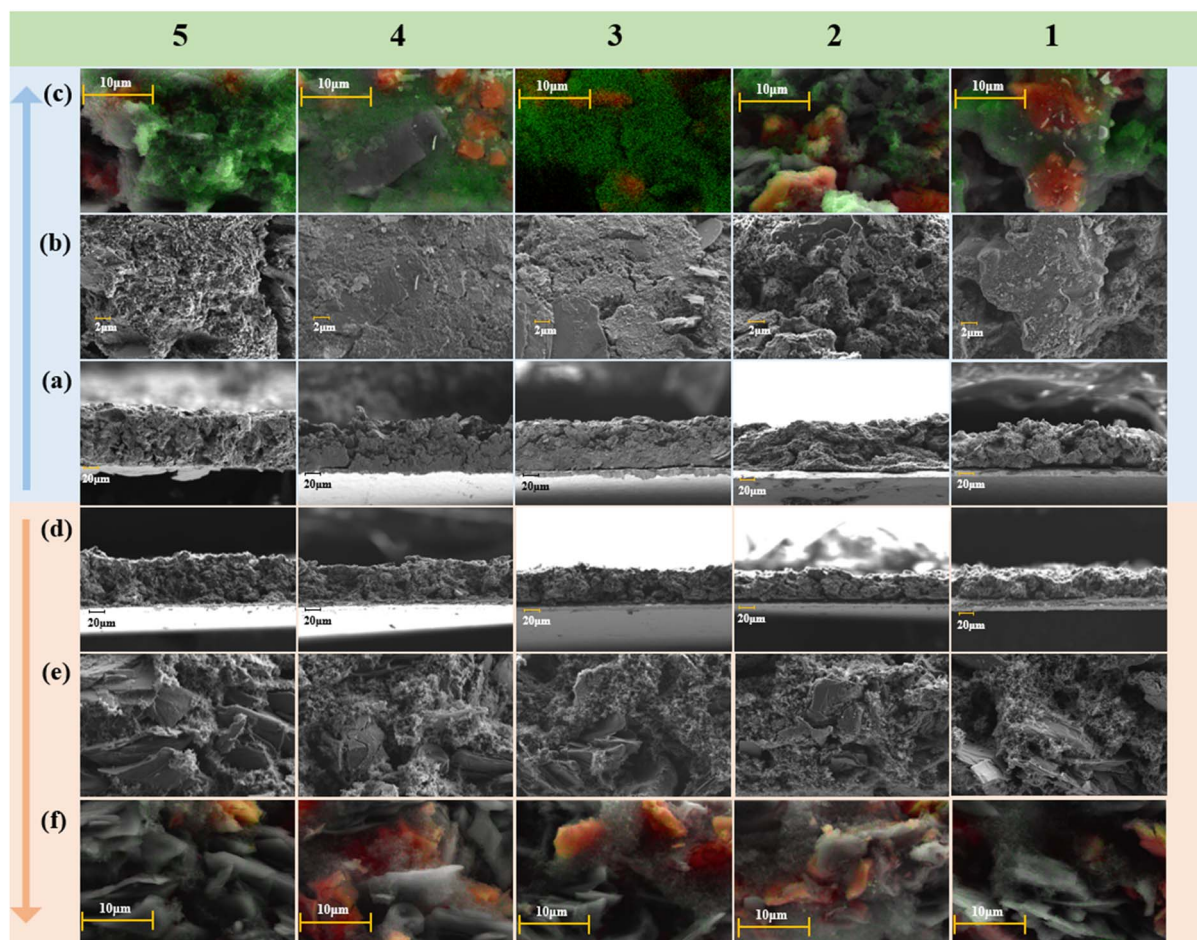

Fig. 7 SEM images and mapping results of Si/C pole pieces with different Si/C loadings for Samples 5–1. After 100 charge–discharge cycles: (a) SEM images of the cross-section. (b) SEM images of the surface. (c) Si (red) and O (green) mapping results for the surface. Fresh (d) SEM images of the cross-section. (e) SEM images of the surface. (f) Si (red) and O (green) mapping results for the surface.

Comparing the appearance of the electrode layers before and after charging and discharging, it can be seen from Fig. 7a and d that there is no significant particle volume expansion during the charge–discharge process, which is the reason for preventing the Si/C material from crushing, separating, and structural damage. The surface structure of the Si/C pole piece

Table 2 Si/O element contents before and after charging–discharging

Sample	After charging–discharging		The fresh	
	Si (at%)	O (at%)	Si (at%)	O (at%)
1	28.88	71.12	68.26	31.74
2	35.38	64.62	68.86	31.14
3	15.06	84.94	64.39	35.61
4	20.03	79.97	63.6	36.4
5	11.06	88.94	54.96	45.04

after charge–discharge cycles (Fig. 7b) is loose, with uneven particle size, distinct layers, and large pores, while Fig. 7e suggests that the microstructure surface of the Si/C composite material before charge–discharge is uniform, with few pores and no obvious cracks. This may be because the original internal structure of the Si/C pole piece is damaged after undergoing charge–discharge cycles, further leading to rapid capacity decay, and the oxygen content also increases with the increase in Si/C loading. Fig. 7c and f indicate that the O element between the samples after charge–discharge cycles and the fresh samples differ greatly. The tested content values also confirmed the phenomenon (Table 2). After disassembly, the electrode layers inevitably come into contact with air and are oxidized, which may be due to the further introduction of oxygen elements.

4. Conclusions

The Si/C pole pieces with five Si/C loadings, namely 1.0 mg cm^{-2}, 1.2 mg cm^{-2}, 2.1 mg cm^{-2}, 2.8 mg cm^{-2}, and 3.2 mg cm^{-2}, have been designed, showing different thicknesses. The battery cells were prepared by matching the Si/C pole pieces, lithium metal sheets, and specialty electrolytes. The galvanostatic charge–discharge tests indicated that an increase in Si/C loading can affect the initial charge–discharge capacity and coulombic efficiency. Additionally, it demonstrates that the Si/C loading has a significant impact on the specific discharge capacity over 100 charge–discharge cycles. The discharge capacity of the Si/C pole pieces is lost due to excessive Si/C loading. The dQ_m/dV curves show that the complex alloying of Si/C alloys is exacerbated by the accumulation of lithium-ions. It is found that the increased Si/C loading can correspondingly lead to the SEI film and charge transfer resistances. Moreover, this work discusses the phase evolution, chemical characteristics, morphology and elemental composition of the Si/C pole piece before and after charging–discharging. Particularly, the results indicate that the characteristics of Si will be weakened by the charge and discharge process.

Data availability

The data that support the findings of this study are available from the corresponding author upon reasonable request and are available in the article.

Author contributions

Y. Y. L.: conceptualization, data curation, investigation and writing – original draft. Z. J. S. and J. W.: conceptualization, formal analysis and supervision. Q. Q. W.: funding acquisition, and writing – review & editing. W. Z. L.: conceptualization, funding acquisition, methodology and writing – review & editing. Q. W.: resources and writing – review & editing. A. Q. W., Y. F. D. and M. K. M.: data curation, investigation and writing – review & editing.

Conflicts of interest

There are no conflicts to declare.

Acknowledgements

References

1 Z. Ma, C. Wang, A. Li, L. Wang, G. Chen, Y. Miao, T. Dang, Y. Wang, E. Chang and T. Fan, *Electrochim. Acta*, 2023, **444**, 141976.

2 K. Park, J. Park, W. M. Seong, K. Yoon, T. Hwang, K. Ko, J. Han, Y. Jaedong and K. Kang, *J. Power Sources*, 2020, **468**, 228369.

3 Q. Pan, J. Zhao, B. Xing, S. Jiang, M. Pang, W. Qu, S. Zhang, Y. Zhang, L. Zhao and W. Liang, *New J. Chem.*, 2019, **43**, 15342–15350.

4 Q. Man, Y. An, C. Liu, H. Shen, S. Xiong and J. Feng, *J. Energy Chem.*, 2023, **76**, 576–600.

5 C. Liu, S. Liu, J. Wang, C. Lin and F. Wu, *Adv. Eng. Res.*, 2018, **146**, 71–75.

6 H. Kim, Y. Yun, Y. C. Lee, M. H. Lee, N. Saito and J. Kang, *Jpn. J. Appl. Phys.*, 2018, **57**, 102B.

7 L. Fan, Q. Li Juan and L. Yan Xia, *Mod. Chem. Ind.*, 2017, **37**(14–18), 20.

8 Q. Shi, J. Zhou, S. Ullah, X. Yang, K. Tokarska, B. Trzebicka, H. Q. Ta and M. H. Rümmeli, *Energy Storage Mater.*, 2021, **34**, 735–754.

9 J. Peng, G. Ji and X. Wang, *J. Power Sources*, 2024, **608**, 234626.

10 Y. Zhang, Y. Zhu, L. Fu, J. Meng, N. Yu, J. Wang and Y. Wu, *Chin. J. Chem.*, 2017, **35**, 21–29.

11 B. C. Huang, L. Y. Tsui, S. Ramki, H. P. Hsu and C. W. Lan, *Heliyon*, 2024, **10**, e33612.

12 D. H. S. Tan, Y. T. Chen, H. Yang, W. Bao, B. Sreenarayanan, J. M. Doux, W. Li, B. Lu, S. Y. Ham and B. Sayahpour, *Energy Environ. Sci.*, 2021, **2103**, 04230.

13 X. Zhang, D. Wang, X. Qiu, Y. Ma, D. Kong, K. Müllen, X. Li and L. Zhi, *Nat. Commun.*, 2020, **11**, 3826.

14 D. Wang, L. Kong, F. Zhang, A. Liu, H. Huang, Y. Liu and Z. Shi, *Appl. Surf. Sci.*, 2024, **661**, 160076.

15 S. Poetke, F. Hippauf, A. Baasner, S. Dörfler, H. Althues and S. Kaskel, *Batteries Supercaps*, 2021, **4**, 1323–1334.

16 X. Shen, Z. Tian, R. Fan, L. Shao, D. Zhang, G. Cao, L. Kou and Y. Bai, *J. Energy Chem.*, 2018, **27**, 1067–1090.

17 M. Khan, S. Yan, M. Ali, F. Mahmood, Y. Zheng, G. Li, J. Liu, X. Song and Y. Wang, *Nano-Micro Lett.*, 2024, **16**, 179.

18 H. F. Andersen, C. E. L. Foss, J. Voje and R. Tronstad, *Sci. Rep.*, 2019, **9**, 14814.

19 X. Xu, X. Mu, T. Huang and A. Yu, *J. Power Sources*, 2024, **614**, 234992.

20 H. Cui, Z. Wang, Y. Jing, X. Li, W. Peng, H. Guo, H. Duan, G. Yan, J. Wang and G. Li, *Mater. Today Energy*, 2024, **46**, 101716.

21 R. Cong, J. Choi, J. Song, M. Jo, H. Lee and C. Lee, *Sci. Rep.*, 2021, **11**, 1283.

22 J. Wang, S. Li, Y. Zhao, J. Shi, L. Lv, H. Wang, Z. Zhang and W. Feng, *RSC Adv.*, 2018, **8**, 666–6666.

23 Y. Ling, P. Zeng, B. Wang, L. Zhang and J. Wang, *J. Mater. Chem. A*, 2024, **12**, 14957–14974.

24 G. G. Eshetu, H. Zhang, X. Judez, H. Adenusi, M. Armand, S. Passerini and E. Figgemeier, *Nat. Commun.*, 2021, **12**, 5459.

25 M. K. Datta and P. N. Kumta, *J. Power Sources*, 2006, **158**, 557–563.

26 J. Sung, J. Heo, D. Kim, H. Gu, Y. Jo, H. Park, J. Park, J. Choi, Y. Ha, D. Kim and J. Park, *NPG Asia Mater.*, 2024, **16**, 53.

27 C. M. Costa, K. J. Merazzo, R. Gonçalves, C. Amos and S. Lanceros-Méndez, *Iscience*, 2021, **24**, 102691.

28 S. Mahmud, M. Rahman, M. Kamruzzaman, M. O. Ali, M. S. A. Emon, H. Khatun and M. R. Ali, *Results Eng.*, 2022, **15**, 100472.

29 H. Zhang, Y. Gao, G. Zhu, T. Tan, C. Liang, S. Hao, C. Zhao, W. Chen and D. Ren, *Chem. Eng. J.*, 2024, **499**, 155759.

30 L. Sun, Y. Liu, R. Shao, J. Wu, R. Jiang and Z. Jin, *Energy Storage Mater.*, 2022, **46**, 482–502.

31 L. Yang, S. Li, Y. Zhang, H. Feng, J. Li, X. Zhang, H. Guan, L. Kong and Z. Chen, *J. Energy Chem.*, 2024, **97**, 30–45.

32 J. K. Lee, K. B. Smith, C. M. Hayner and H. H. Kung, *Chem. Commun.*, 2010, **46**, 2025–2027.

33 Z. Luo, D. Fan, X. Liu, H. Mao, C. Yao and Z. Deng, *J. Power Sources*, 2009, **189**, 16–21.

34 Z. Xiao, C. Wang, L. Song, Y. Zheng and T. Long, *J. Solid State Electrochem.*, 2022, **26**, 1125–1136.

35 S. M. Liang, F. Taubert, A. Kozlov, J. Seidel, F. Mertens and R. Schmid-Fetzer, *Intermetallics*, 2017, **81**, 32–46.

36 Z. Feng, W. Peng, Z. Wang, H. Guo, X. Li, G. Yan and J. Wang, *Int. J. Miner. Metall. Mater.*, 2021, **28**, 1549–1564.

37 Y. Kubota, M. C. S. Escaño, H. Nakanishi and H. Kasai, *J. Alloys Compd.*, 2008, **458**, 151–157.

38 M. Gu, Z. Wang, J. G. Connell, D. E. Perea, L. J. Lauhon, F. Gao and C. Wang, *ACS Nano*, 2013, **7**(7), 6303–6309.

39 L. Ye, Y. Lu, Y. Wang, J. Li and X. Li, *Nat. Mater.*, 2024, **23**, 244–251.

40 Y. Yang, J. G. Ren, X. Wang, Y. S. Chui, Q. H. Wu, X. Chen and W. Zhang, *Nanoscale*, 2013, **5**, 8689–8694.

41 J. Wei, C. M. Qin, H. Su, J. M. Wang and X. T. Li, *Carbon*, 2020, **170**, 685.

42 S. Liu, L. Zhou, J. Han, K. Wen, S. Guan, C. Xue, Z. Zhang, B. Xu, Y. Lin and Y. Shen, *Adv. Energy Mater.*, 2022, **12**, 2200660.

43 J. Song, S. Chen, M. Zhou, T. Xu, D. Lv, M. L. Gordin, T. Long, M. Melnyk and D. Wang, *J. Mater. Chem. A*, 2014, **2**, 1257–1262.

44 B. Zhang, L. Tong, L. Wu and Y. Hu, *J. Phys.: Conf. Ser.*, 2021, **2079**, 12005.

45 Z. Qinglin, W. Mingxia, C. Si and Y. Chongyang, *Electron. Compon. Mater.*, 2019, **38**, 6.

46 Y. Shi, S. Xu, Y. Yang, S. Slizovskiy, S. V. Morozov, S. K. Son, S. Ozdemir, C. Mullan, J. Barrier, J. Yin, A. I. Berdyugin, B. A. Piot, T. Taniguchi, K. Watanabe, V. I. Fal'Ko, K. S. Novoselov, A. K. Geim and A. Mishchenko, *Nature*, 2020, **584**, 210–214.

47 X. Shen, Z. Tian, R. Fan, L. Shao, D. Zhang, G. Cao, L. Kou and Y. Bai, *J. Energy Chem.*, 2018, S1746544188.

48 J. Nanda, M. K. Datta, J. T. Remillard, A. O Neill and P. N. Kumta, *Electrochem. Commun.*, 2009, **11**, 235–237.

49 V. Etacheri, O. Haik, Y. Goffer, G. A. Roberts, I. C. Stefan, R. Fasching and D. Aurbach, *Langmuir*, 2012, **28**, 965–976.

50 Y. X. Yin, S. Xin, L. J. Wan, C. J. Li and Y. G. Guo, *J. Phys. Chem. C*, 2011, **115**, 14148–14154.

51 Z. Zhao, Z. Wu, W. Yang, X. Liu and W. Jiang, *Acta Sci. Nauralium Univ. Pekin.*, 2006, **42**, 39–43.